Spatial Resolution Enhancement of Satellite Hyperspectral Data via Nested Hypersharpening With Sentinel-2 Multispectral Data

Luciano Alparone, Alberto Arienzo, and Andrea Garzelli, *Senior Member, IEEE*

***Abstract*—This article presents an original method for the spatial resolution enhancement of satellite hyperspectral (HS) data by means of the Sentinel-2 visible and near infrared (VNIR) and short-wave infrared bands at 10 and 20 m spatial resolution. Presently, HS data are available from PRISMA (Italian acronym for HS precursor of the application mission) and Environmental Mapping and Analysis Program (EnMAP): both map the spectral interval of the solar radiation onto 240 and 224 bands, respectively, with 10 and 6.5/10 nm widths. A 5 m × 5 m panchromatic (PAN) band is also acquired by PRISMA. When the PAN band is unavailable, or better, the higher spatial resolution sharpening band is not unique, advantage can be taken from the hypersharpening protocol. First, the 20-m bands of Sentinel-2 are hypersharpened to 10 m by means of the four 10-m VNIR bands of the same instrument. Then, the 10-m hypersharpened bands of Sentinel-2 are used to sharpen the 30-m bands of PRISMA at 10 m as well, still according to the hypersharpening protocol. Eventually, the 10- m hypersharpened bands are pansharpened at 5 m by means of the PAN image, if available. Results show that for PRISMA the nested hypersharpening followed by pansharpening is better than plain HS pansharpening, both visually and according to full-scale indexes of spectral and spatial consistence. For EnMAP data, in which the PAN image is missing, the improvement of the fused data with respect to the original EnMAP and Sentinel-2 data has been quantified by means of two novel statistical indexes capable of measuring the spatial and intersensor consistencies between sharpened and sharpening data.**

***Index Terms*—Environmental mapping and analysis program (EnMAP), hypersharpening, hyperspectral (HS) image data, HS pansharpening, PRISMA, Sentinel-2.**

I. Scenario and Motivations

THE availability of hyperspectral (HS) datasets taken from space, dates back to almost a quarter of century ago, with the pioneering push-broom Hyperion spectrometer on the Earth Observation-1 (EO-1) satellite, launched by NASA. EO-1 was also equipped with a 10-band multispectral (MS) scanner, including a 10-m panchromatic (PAN) band [1]. Unfortunately, Hyperion featured a narrow swath (7.7 km), because of technological limitations, and experienced serious miscalibration problems, few years after its launch, a problem that new-generation spaceborne imaging spectrometers have brilliantly solved through an onboard calibration system based on fixed stars.

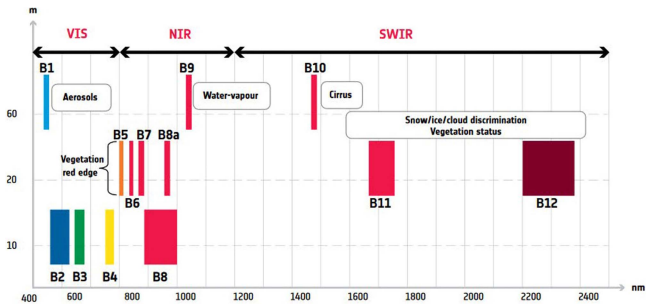

Fig. 1. Sentinel-2 layout of spectral bands.

Almost 20 years later, technological advances lead to launch of two HS missions from as many European countries: The Italian Space Agency's PRISMA (Italian acronym for HS Precursor of the Application Mission) [2], and the Environmental Mapping and Analysis Program (EnMAP) [3], managed by the German DLR Agency. The main characteristics of the two missions and related data products are as follows. PRISMA was launched on 22 March, 2019, and is equipped with: 1) an HS sensor with a spatial resolution of 30 m × 30 m and a spectral resolution of 10 nm ranging from 400–2500 nm, and 2) a PAN instrument with a narrow bandwidth of (450–700) nm and a spatial resolution of 5 m × 5 m. EnMAP was launched on 1 April, 2022, and is equipped with an HS imager capable of resolving 224 spectral bands from 420–2450 nm with spectral resolutions of 6.5 nm in visible and near infrared (VNIR) and 10 nm in short-wave infrared (SWIR) and a ground resolution of 30 m × 30 m.

In parallel, the Sentinel-2 twin satellite constellation (2A and 2B) of the European Space Agency provides MS data in the VNIR and SWIR wavelengths at decametric spatial resolution, with global coverage of the Earth in few days. Among the Sentinel-2 bands, whose layout is shown in Fig. 1, B5–B7, in the red-edge (RE) region, B11 and B12, in the SWIR region, and B8a, a narrow-band NIR centered at 865 nm, are provided

Manuscript received 20 December 2023; revised 20 April 2024; accepted 21 May 2024. Date of publication 29 May 2024; date of current version 14 June 2024. A preliminary version of this article has been presented at the 2023 IEEE Geoscience And Remote Sensing Symposium, Pasadena, CA, USA. *(Corresponding author: Andrea Garzelli.)*

Luciano Alparone is with the Department of Information Engineering, University of Florence, 50139 Florence, Italy (e-mail: luciano.alparone@unifi.it).

Alberto Arienzo is with the National Research Council, Institute of Methodologies for Environmental Analysis, 85050 Tito Scalo, Italy, and also with the Department of Information Engineering, University of Florence, 50139 Florence, Italy (e-mail: alberto.arienzo@imaa.cnr.it).

Andrea Garzelli is with the Department of Information Engineering and Mathematics, University of Siena, 53100 Siena, Italy (e-mail: andrea.garzelli@unisi.it).

Digital Object Identifier 10.1109/JSTARS.2024.3406762

at 20 m spatial resolution. The VNIR bands, specifically B2, B3, B4, and B8, have higher spatial resolution, 10 m. The three 60-m bands, B1, B9, and B10 are less relevant for EO and are mainly used for studies of atmosphere, to infer the content of aerosols, water vapor and ice, respectively. The difference in spatial resolutions is a consequence of the fundamental tradeoff in the design of electro-optical systems between spatial resolution, spectral resolution, and radiometric sensitivity [4]. Thus, MS resolution enhancement may improve the spatial resolution of the Sentinel-2 bands acquired at 20 and 60 m.

MS resolution enhancement refers to the joint processing of the data in order to synthesize an image product that ideally exhibits the spectral characteristics of the observed multiband image at the spatial resolution, and hence spatial sampling, of the higher resolution dataset. When this higher resolution image is a PAN image, spatial enhancement is referred to as MS pansharpening [5], [6]; when a PAN band is unavailable or equivalently the sharpening band is not unique, hypersharpening denotes the sharpening of the less spatially resolved bands by means of a suitable combinations of the more spatially resolved bands, typically in the VNIR wavelengths [7], in order to maximize a similarity function, either global or local, between the low-pass version of the sharpening image, which is the synthesized PAN, and the lower resolution band that shall be sharpened. The rationale for hypersharpening lies in finding the spatial/spectral patterns between the sharpening and sharpened bands, as originally devised for HS data compression [8]. Alternatively, it may be brought back to the concept of blind source separation [9]. Originally devised for single-platform data [7], [10], hypersharpening has been extended to multiplatform data [11], [12]. A preliminary version of the present study concerns only the PRISMA data [13].

Depending on the sharpening protocol, the normalized spectral indexes, e.g., [14], obtained from sharpened data may be spatially enhanced or not [15]. If the sharpening band is unique, as happens with pansharpening, it can be proven that there is no increase in spectral information at the finer spatial scale [16]. The case of hypersharpening, in which the sharpener is different for each lower resolution band, has never been investigated in this sense. Specifically, the Sentinel-2 bands in the RE regions, namely, B5 and B6, with a 15-nm spectral width, and B7, with a 20-nm width (see Fig. 1), are provided at 20 m spatial resolution. Thus, MS hypersharpening may improve the spatial resolution of the Sentinel-2 bands acquired at 20 and 60 m and the derived spectral indexes, specifically those computed from the RE bands, suitable for studies on vegetation [17], [18].

If an auxiliary dataset, taken from another platform, whose instruments span the same wavelengths as the HS sensor, is available, the relatively high ratio between the scales of the HS and PAN data (30 m HS, 5 m PAN) can be accommodated in several sharpening steps, each with scale ratio two or three at most. In this work, we will show that multistep fusion with an auxiliary sensor is more accurate in spectral terms than single-step fusion with data from a unique platform; the spatial accuracy, dictated by the PAN image, is pretty comparable. For the specific case of PRISMA and Sentinel-2 data, it will be shown that a three-step procedure produces 5 m HS data with higher spectral quality than those obtained by straightforward pansharpening of the 30-m PRISMA data. This is possible by first hypersharpening the 20-m Sentinel-2 bands at 10 m spatial resolution, then enhancing the spatial resolution of PRISMA data to 10 m by means of the hypersharpened Sentinel-2 images, and finally by applying pansharpening to the previously obtained 10 m HS data. In the case of EnMAP data, the final pansharpening step is omitted, due to the absence of a PAN image. The latter case can be regarded as an MS-to-HS fusion, for which an approach based on spectral profiles has recently been pursued [19].

The rest of this article is organized as follows. Section II reviews the hypersharpening protocol, with specific reference to the scales and scale ratios of Sentinel-2. Section III illustrates the proposed approach for multiplatform fusion data based on nested hypersharpening stages. Section IV presents results of nested hypersharpening on PRISMA and EnMAP datasets and discusses full-scale quality assessment. Finally, Section V concludes this article, where possible applications to the temporal monitoring of vegetated areas are highlighted.

II. Review of Hypersharpening

While pansharpening increases the geometric resolution of a multiband image by means of a PAN observation of the same scene with greater resolution, whenever the sharpening image is not unique, hypersharpening deals with the synthesis of a unique sharpening image, the source of the spatial details, to obtain the best-fused products [7]. This synthetic PAN is generally different for each band that is to be sharpened.

Let $\{\mathbf{M}_k\}_{k=1,\ldots,N}$ denote the higher resolution bands, e.g., the four 10-m VNIR bands of Sentinel-2, $\{\mathbf{H}_i\}_{i=1,\ldots,M}$ the lower resolution bands, e.g., the three RE, the narrowband NIR, and the two SWIR bands of Sentinel-2, all at 20 m spatial scale, and R the ratio between the spatial scales of $\mathbf{H}$ and $\mathbf{M}$ ($N = 4$, $M = 6$, and $R = 2$, for Sentinel-2). The enhancing band $\mathbf{P}_i^*, i = 1, \ldots, M$, of the ith lower resolution band, $\mathbf{H}_i$, is synthesized according to the following procedure.

First, the $\mathbf{M}_k$ bands are low-pass filtered with a cutoff frequency $1/R$, providing the bands $\overline{\mathbf{M}}_k$ degraded at the resolution of the bands that are being sharpened. Then, the relationship between the lower resolution bands interpolated by R, $\widetilde{\mathbf{H}}_i$, and $\overline{\mathbf{M}}_k$ is modeled through a multivariate linear regression

$$\widetilde{\mathbf{H}}_i = w_0^{(i)} + \sum_{k=1}^{N} w_k^{(i)} \cdot \overline{\mathbf{M}}_k + \epsilon_i \qquad i = 1, \ldots, M \tag{1}$$

in which ϵ_i is the space-varying residue. The set of optimal space-constant weights, $\{\widehat{w}_k^{(i)}\}_{k=0,\ldots,N}$, is calculated as the minimum MSE (MMSE) solution of (1). The weights, $\widehat{w}_k^{(i)}$, are used to synthesize the set of enhancing bands, $\{\mathbf{P}_i^*\}_{i=1,\ldots,M}$

$$\mathbf{P}_i^* = \widehat{w}_0^{(i)} + \sum_{k=1}^{N} \widehat{w}_k^{(i)} \cdot \mathbf{M}_k \qquad i = 1, \ldots, M. \tag{2}$$

Finally, the sharpened bands $\widehat{\mathbf{H}}_i$, at a resolution of 10 m for Sentinel-2, are computed by applying a contrast-based fusion algorithm to $\widetilde{\mathbf{H}}_i$ and $\mathbf{P}_i^*$

$$\widehat{\mathbf{H}}_i = \widetilde{\mathbf{H}}_i \cdot \frac{\mathbf{P}_i^*}{\overline{\mathbf{P}}_i^*}, \quad i = 1, \ldots, M \tag{3}$$

in which $\overline{\mathbf{P}}_i^*$ is the low-pass-filtered version of $\mathbf{P}_i^*$, or, equivalently

$$\overline{\mathbf{P}}_i^* = \widehat{w}_0^{(i)} + \sum_{k=1}^{N} \widehat{w}_k^{(i)} \cdot \overline{\mathbf{M}}_k \qquad i = 1, \ldots, M. \tag{4}$$

The three 60-m bands of Sentinel-2 may be sharpened either starting from the six 20-m bands, before the 20 to 10 m sharpening step described in (1)–(4) is performed, or directly sharpened from the set of 10-m bands, original (B2, B3, B4 and B8) and previously hypersharpened (B5, B6, B7, B8a, B11 and B12).

Note that, for Sentinel-2, the sharpening bands and the sharpened bands are simultaneously acquired by the same platform, while, for very/extremely high resolution MS scanners, e.g., WorldView-3, in which four instruments with three different resolutions are present [10], such an acquisition is not simultaneous but is made from different positions along the orbit; this may lead to local shifts between the two datasets [20], in the presence of some relief of the ground. The absence of residual spatial shifts between the datasets entails the use of fusion methods based on multiresolution analysis (MRA), either separable [21] or not [22], of the sharpening image. Such methods are also recommended for merging data coming from different platforms [23].

The coefficients of determination of the multivariate regressions in (1) determine the histogram matching between each of the low-resolution bands and the enhancing image synthesized from the 10-m VNIR bands [24]. It is noteworthy that the use of a multivariate regression to synthesize the sharpening band makes the method independent of the data format [25], which is either floating point or packed fixed point. However, while the math derivation of the sharpening bands does not depend on the physical format of the data, e.g., spectral radiance or surface reflectance, the fusion rule in (3), derived from the radiative transfer model [26], would assume that all band data are in the surface reflectance format.

The surface reflectance is a level two (L2) product and is usually distributed for global-coverage systems, such as Operational Land Imager (OLI) and Sentinel-2, when an instrument network is available for atmospheric measurements [27], which are usually carried out by means of LiDAR instruments, exploiting the interaction with the atmosphere of laser beams [28]. If only the spectral radiance format is available, the band data should be corrected for haze, that is, each should be diminished by the corresponding term of atmospheric path radiance, a.k.a. haze [29], when used in (3). According to the radiative transfer model [26], a low-resolution surface reflectance image, obtained from the dehazed spectral bands as a ratio of spectral radiances to their average, is sharpened by the high-resolution PAN image. While atmospheric transmittances and solar irradiance cancel each other in the ratio, the haze terms should be preliminarily estimated and removed. Path-radiance estimation may follow image-based approaches [30], [31] or rely on radiative transfer models of the atmosphere and its constituents [32], as well as knowledge of acquisition parameters, such as actual Sun–Earth distance, solar zenith angle, and satellite platform observation angle. The haze term is trivially zero for data in surface reflectance format, whenever they are available. For both PRISMA and EnMAP datasets, L2 surface reflectance products are usually available.

III. Flowchart of the Proposed Method

The proposed sharpening method is composed of three steps, graphically described in Fig. 2. The number of steps is equal to the overall number of different resolutions concerned minus one: 30 m (PRISMA and EnMAP HS), 20 m (medium-resolution Sentinel-2 bands), 10 m (high-resolution Sentinel-2 bands), and 5 m (PRISMA PAN). For conventional pansharpening with only two datasets, the number of steps is trivially one. The three 60-m bands of Sentinel-2 have been intentionally discarded because their resolution is lower than that of the HS datasets.

The inner step only concerns Sentinel-2 data. Attention is focused on the three RE bands, whose relevance to the analysis of vegetation characteristics has been largely recognized [14], on the narrow NIR band B8a and on the two SWIR broad bands. Originally produced at 20 m resolution, all these bands are hypersharpened by means of the four 10-m VNIR bands (see Fig. 1).

1) The six Sentinel-2 bands at 20 m resolution are hypersharpened to 10 m by means of a combination of the four 10-m VNIR bands, following (1)–(4).
2) The N 30-m HS bands, either PRISMA or EnMAP, are hypersharpened at 10 m by means of a combination of the 10-m Sentinel-2 bands, four original and six hypersharpened, as described in Step 1). Each 30-m HS band is spatially enhanced at 10 m according to the hypersharpening protocol in (1)–(4).
3) For PRISMA datasets only, the N 10-m HS bands obtained from Step 2) are pansharpened to 5 m by means of any existing pansharpening method, either based on component substitution (CS) or on MRA, using the available 5 m PAN observation of PRISMA as sharpening image.

Note the presence of two nested hypersharpening boxes: the hypersharpening of HS data is achieved by means of MS data that have been previously hypersharpened as well.

IV. Experimental Results

A. Datasets

We have collected level-2D HS + PAN images acquired by PRISMA on 7 November, 2020 over the city of Bologna, Italy, and its surroundings. The level-2D product refers to the geocoded surface reflectance data product. Atmospheric water vapor absorption bands, low signal-to-noise ratio (SNR) bands (due to low quantum efficiency), and bands affected by severe striping effects (due to a temporarily unbalanced response of some of the VNIR or SWIR detectors) have been removed. Sentinel-2 geocoded surface reflectance data have also been collected. The acquisition over the same area was taken few days later, on 11 November, 2020. A residual space-varying misalignment between the HS bands and the PAN image of PRISMA and of the PRISMA data with the Sentinel-2 bands has been corrected by local correlation computation and nonrigid transformation [33].

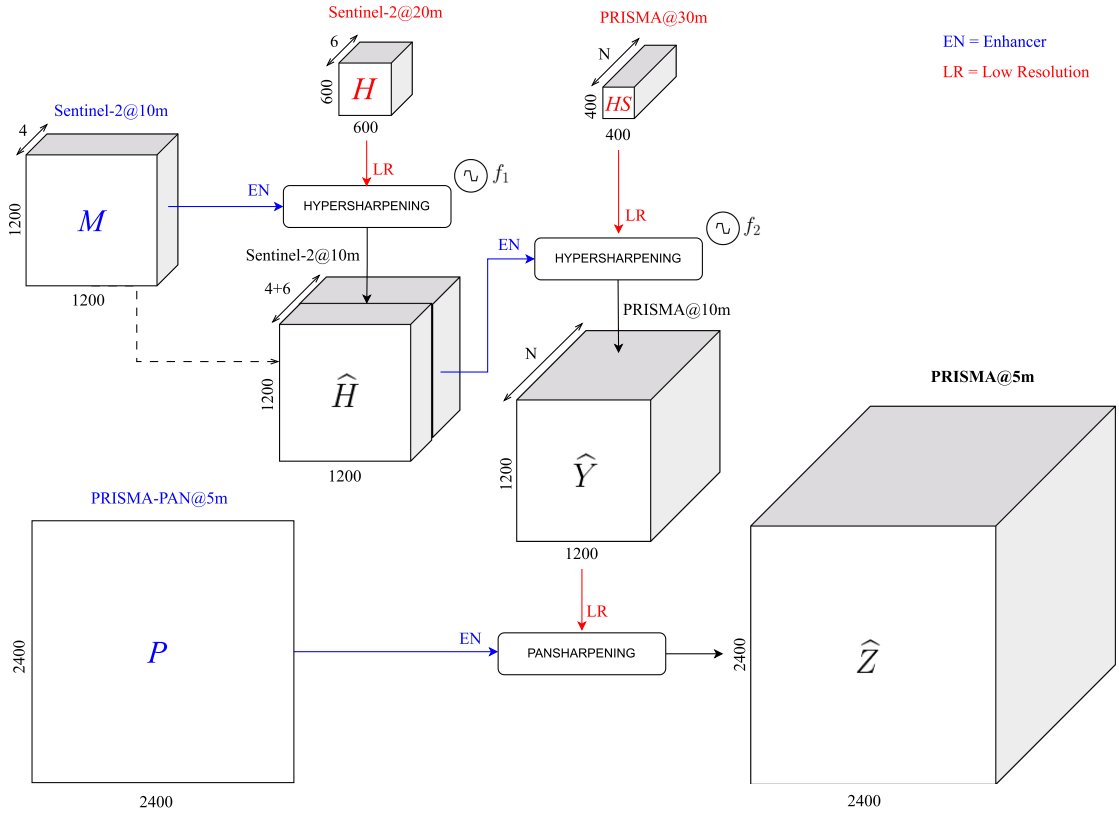

Fig. 2. Flow diagram of the proposed HS/Sentinel-2 sharpening method, for the case of PRISMA data (HS+PAN). For EnMAP data, the pansharpening stage is missing and the final product is $\widehat{Y}$.

The EnMAP dataset was acquired on 10 August, 2022 over the site of Groningen, The Netherlands. Data were atmospherically corrected and geocoded by bilinear interpolation and UTM/WGS84 projection. The data format is normalized remote sensing reflectance on 224 spectral bands. After discarding the water absorption bands, the EnMAP data cube is made up of 213 bands. The Sentinel-2 dataset was acquired by the Sentinel-2B twin satellite on 10 August, 2022 over the Groningen site. The data product is the UTM/WGS84 projected Level-2 A (atmospherically corrected surface reflection images). Due to a satellite acquisition angle of 11° for EnMAP, there is a difference in the acquisition times of the two images of about 1 h, whereas the acquisition day is the same.

B. Setup

For PRISMA datasets only, two fusion methods, GSA [34] based on CS and AWLP [35] based on "à trous" MRA [36] have been chosen for single-step pansharpening and for the final pansharpening step after the two nested hypersharpening steps. The typology of the method, either CS or MRA, has implications on tolerance to misregistration [6]. In fact, local space-varying shifts between PRISMA HS and PAN may be magnified by the presence of auxiliary sensor according to a triangular inequality: shift(HS,PAN) $\leq$ shift(HS,MS) + shift(MS,PAN), with obvious meaning of symbols.

C. Assessment

Even though many efforts have been done since the problem has been originally stated [37], quality assessments of fusion products remains an open problem [38], [39]. Objective evaluations at full scale have been carried out in terms of separate measurements of the spectral consistency of the fused HS data to the original HS data [40]. Full-scale quality evaluations should avoid spectral and spatial consistency indexes that have been found to be sensitive to MS-to-PAN misregistration [41]. In this light, the spectral distortion of the QNR protocol, namely, D_λ, and the spatial distortion, D_s^*, based on the multivariate regression of the sharpened bands to the PAN image [42] have been coupled to produce a unique quality index, QNR*, normalized in [0,1]

$$\mathbf{QNR}^* = (1 - D_\lambda)(1 - D_s^*) \tag{5}$$

in which the spatial consistency factor, $1 - D_s^*$, reflects the ability of the sharpened bands to synthesize back the sharpening band and is defined as the coefficient of determination, R^2, of the MMSE solution of the multivariate regression of $\widehat{\mathbf{H}}_i$ toward either $\mathbf{P}$ or $\mathbf{P}_i^*$ (2), for pansharpening or hypersharpening, respectively. Thus, the definition of spatial consistency, $1 - D_s^*$, entails its extension to hypersharpening, for which the sharpening image is not unique.

Eventually, if $\mathbf{P}_i^*$ is replaced with $\widehat{\mathbf{M}}_i$, an intersensors' consistency index can be defined as the ability of the sharpened bands of the lower spatial resolution instrument to synthesize back each of the bands of the higher resolution instrument

$$\mathbf{M}_i = \hat{\alpha}_0^{(i)} + \sum_{k=1}^{M} \hat{\alpha}_k^{(i)} \cdot \widehat{\mathbf{H}}_k + \epsilon_i \qquad i = 1, \ldots, N \tag{6}$$

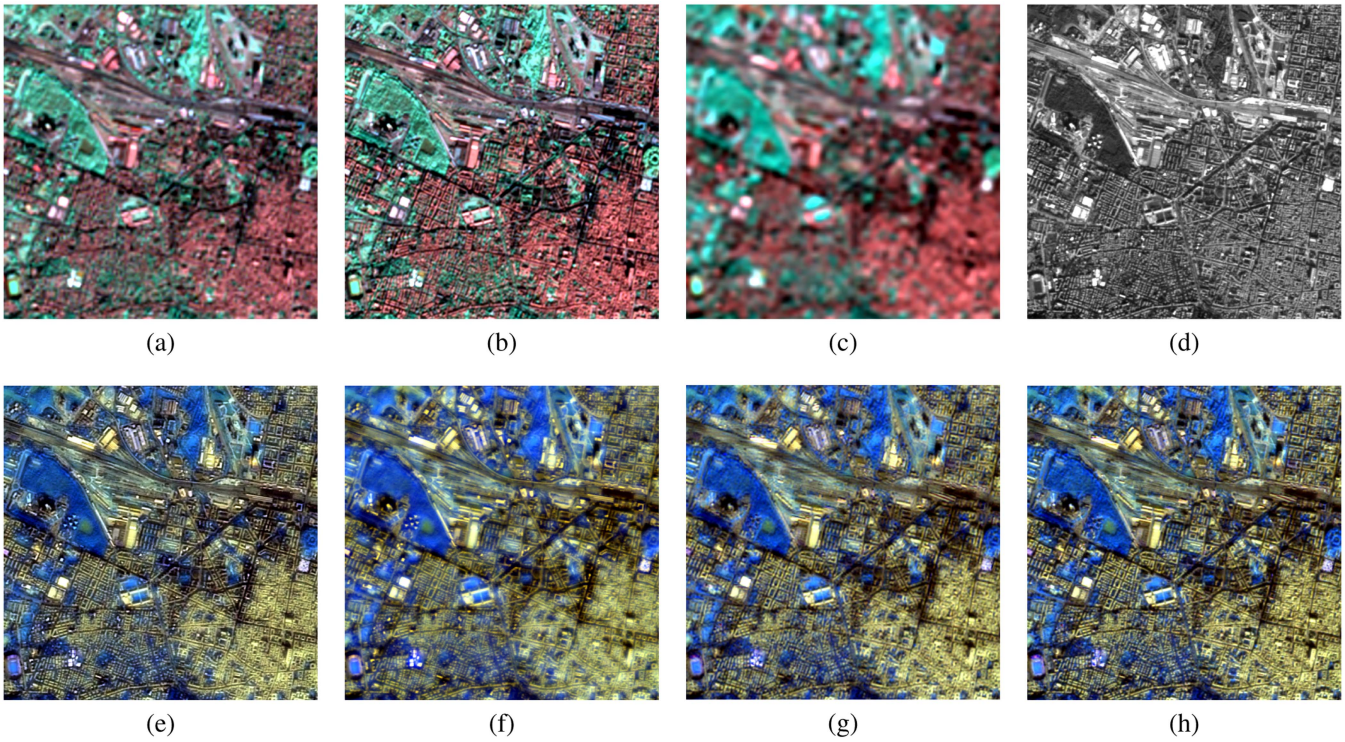

Fig. 3. 3 km ×3 km portion of Sentinel-2/PRISMA acquisitions over the city of Bologna: (a) composition of (1375, 865, 740 nm) as (R, G, B) color channels of 20 m original Sentinel-2 bands, (b) same color composition of 20 m Sentinel-2 bands hypersharpened to 10 m, (c) (1400, 866, 749 nm) color composition of 30 m original PRISMA bands, and (d) 5 m PAN PRISMA band. Second row, (2094, 1775, 1029 nm) R-G-B color compositions of: (e) 5 m AWLP-pansharpened PRISMA, (f) 5 m GSA-pansharpened PRISMA, (g) PRISMA hypersharpened by 10 m Sentinel-2, and (h) 10 m hypersharpened PRISMA pansharpened by 5 m PAN band.

in which $\{\hat{\alpha}_k^{(i)}, k = 1, \ldots, M; i = 0, \ldots, N\}$ are the coefficients of the least squares (LS) solutions of (6). For each of the sharpening bands, $\mathbf{M}_i$, the R^2 of the LS fit is a normalized measure of intersensor consistency. The latter is the most important property of hypersharpening, in which both datasets feature a spectral diversity, which should be preserved after the fusion.

D. Simulations

1) PRISMA: Fig. 3(a)–(d) reports false color compositions of original 20 m Sentinel-2, 20 m Sentinel-2 hypersharpened at 10 m, original 30 m PRISMA, and grayscale 5 m PAN image, respectively. The color composition displays the SWIR wavelengths as the red channel, the NIR spectrum as the green channel, while the upper RE interval is mapped onto the blue channel. This choice considers bands that are available on both instruments. The goal is to properly enhance the vegetated regions in Fig. 3(c) by means of the texture information in Fig. 3(a), especially noticeable after hypersharpening in Fig. 3(b), because the original PAN in Fig. 3(d) lacks spatial information. In fact, the narrow-band PAN of PRISMA (450–700 nm) is unable to sharpen vegetated regions, which mostly reflect the radiation beyond the visible, in the NIR wavelengths.

The visual results of fusion in Fig. 3(e)–(f), displayed in a color composition of bands that are not present in Sentinel-2, (R = 2094 nm, G = 1775 nm, and B = 1029 nm) show that the Sentinel-2-enforced fusion of PRISMA data provides an extra value. Plain, i.e., single-step, pansharpening, either MRA (AWLP) in Fig. 3(e) or CS (GSA) in Fig. 3(f) appears quite different to one another. AWLP is unrealistically overenhanced, except on vegetation. GSA provides enhancement on the textured urban areas, but leaves the vegetated areas almost unchanged, because its regression-based intensity component recasts the PAN image, and hence the detail injected on vegetation is practically zero. The proposed method first calculates the 10-m auxiliary data, i.e., the hypersharpened Sentinel-2 bands, then merges them with the PRISMA data in Fig. 3(c) to produce the intermediate result of Fig. 3(g).

Eventually, the final product in Fig. 3(h) is achieved by merging Fig. 3(g) with the PAN image in Fig. 3(d). The proposed method provides a 5-m final fusion product more detailed than the single-step GSA [see Fig. 3(f)] and more accurate than the single-step AWLP [see Fig. 3(e)], with noticeable spectral preservation. The results of the proposed three-step nested procedure are not displayed for AWLP, because of puzzling artifacts due to misalignment among the datasets, which are three instead of two.

The objective evaluations at the full spatial scale are reported in Table I. The entry EXP is the interpolated PRISMA image [see

TABLE I
FULL-RESOLUTION DISTORTION/QUALITY INDEXES OF PRISMA–BOLOGNA

	D_λ	D_s^*	QNR*
EXP	**0**	0.2889	0.7111
AWLP	0.0976	0.0491	0.8581
GSA	0.0649	**0.0121**	0.9238
Nested AWLP	0.0987	0.0527	0.8538
Nested GSA	**0.0514**	0.0139	**0.9354**

Best values are boldfaced.

Fig. 4. 15 km × 6 km EnMAP acquisition: (647-551-468) nm composition at 30 m spatial resolution, interpolated at 10 m.

Fig. 5. 15 km × 6 km Sentinel-2B acquisition: B4–B3–B2 composition at 10 m spatial resolution.

Fig. 3(c)] and is the reference of spectral quality, the distortion D_λ being identically zero. D_λ is rather high for AWLP and nested AWLP, considerably lower for GSA and even lower for the nested GSA, which recovers spectral information from the Sentinel-2 data. The spectral distortion D_s^*, which is trivially the highest for EXP, is much lower for GSA than for AWLP. The nested procedure, however, slightly increases D_s^*, because the reference of spatial quality is the original PAN and any auxiliary datasets introduce a disturbance into the fusion product, because the textured vegetation in the fusion product is not present in the PAN image. Nevertheless, the advantage in spectral terms is greater than the drawback in spatial terms, and the cumulative score attains the best score for the proposed nested GSA.

We wish to remark, however, that the straightforward extension of full-scale consistency indexes suitable for pansharpened data may not be fully adequate to describe the quality of hypersharpened data, because the intermediate spatial enhancement introduced by the auxiliary sensor, Sentinel-2 in the present case, is likely to lower the spatial consistency toward PAN. Therefore, in the subsequent tests that do not involve a PAN image, intersensor consistency measures will be reported, as defined in Section IV-C.

2) EnMAP: The EnMAP dataset highlights the characteristics of hypersharpening better than the PRISMA dataset. First, the consistency of the spectral signatures acquired by the HS (EnMAP) and MS (Sentinel-2) instruments is evidenced in Figs. 4 and 5, showing true RGB color compositions of the test area, as imaged by the two instruments. The original L2 data product is displayed at the native resolution for Sentinel-2, with an interpolation by three for EnMAP. The match of color hues between the two instruments is excellent, thereby revealing that instrumental and atmospheric corrections were effectively performed, also because there is only an hour difference between the two acquisitions.

The inner step of hypersharpening, performed only on the Sentinel-2 dataset, is reported in Fig. 6. Three 20-m bands in

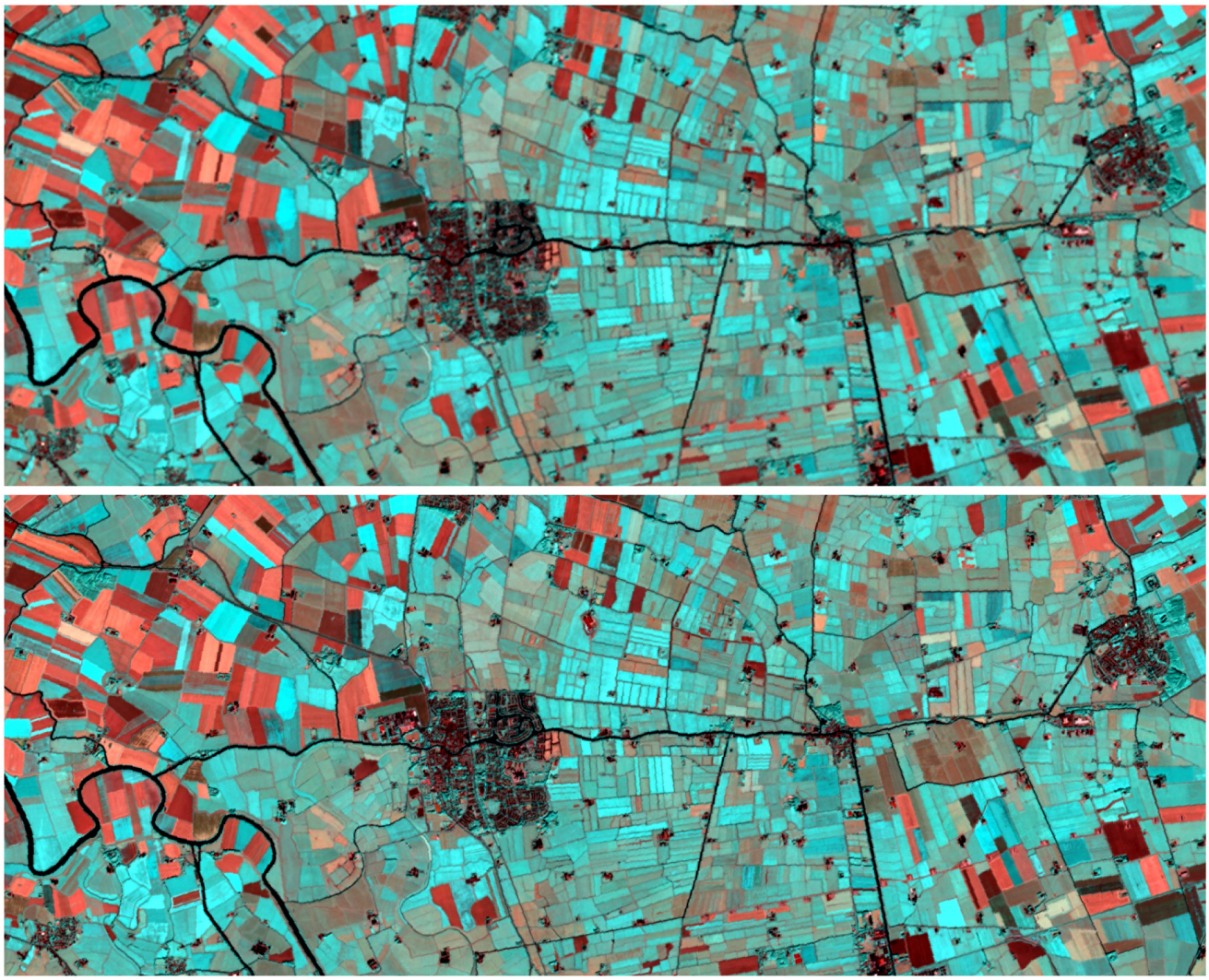

Fig. 6. B11–B8a–B7 Sentinel-2 compositions: 20 m originals interpolated (top) at 10 m and hypersharpened (bottom) at 10 m.

the upper RE, NIR, and SWIR wavelengths are hypersharpened at 10 m by means of the four 10-m VNIR bands. In addition to the fidelity of the color signatures, the increased sharpness, especially noticeable in urban settlements, is impressive for a 2:1 scale ratio.

Eventually, the outer step of hypersharpening, concerning 30 m original EnMAP data and 10 m Sentinel-2 bands, six of which have previously been hypersharpened at 10 m, is shown in Fig. 7, for a color composition of bands spanning the empty gap of the MS instrument, if we exclude the 60-m bands that have not been considered in this study. Sharpening is now even more noticeable, because the scale ratio is 3:1 instead of 2:1. The geometric sharpness and spectral fidelity are even more surprising, because they come from separate datasets of different instruments, without any spectral overlap. We cannot help noticing the excellent spatial alignment of the two datasets, simply delivered in geocoded format, without any further geometric correction by users. This is possible because the test site is perfectly flat.

To provide quantitative insights in the nature of the proposed multiplatform fusion procedure, we present three statistical indexes, two of which have been specifically designed for the task of hypersharpening. The first index is known in the literature [7] and is the root-mean-square error (RMSE) between the original HS band and the sharpened HS band after the spatial detail has been removed by means of a Gaussian low-pass filter, with cutoff at one-third of the Nyquist frequency, for a 3:1 scale ratio. The RMSE is normalized (NRMSE) to the mean of the original HS band and plotted versus the wavelength. Fig. 8 shows that this error is less than 2% in the NIR spectrum, around 3% in the visible wavelengths, and slightly higher than 2% in the right part of the reflective spectrum, with three pronounced peaks corresponding to the two water vapor absorption peaks and the rightmost edge of the SWIR interval, in which the quantum efficiency of the detector quickly decays. Absorption and detector inefficiency determine a marked decrease in SNR and a loss of consistency of the fusion product to its noisy original. Nevertheless, NRMSE is practically always lower than 5% and lower than 3% on average, indicating a good consistency of the HS data fused with the original ones. We recall that the EnMAP dataset contains almost all the bands that have been acquired (only 11 have been discarded), presumably, due to an extremely dry acquisition day.

The second index is a generalization of D_s^* [20], to the case of multiple (synthetic) PAN images. Instead of a unique value, the

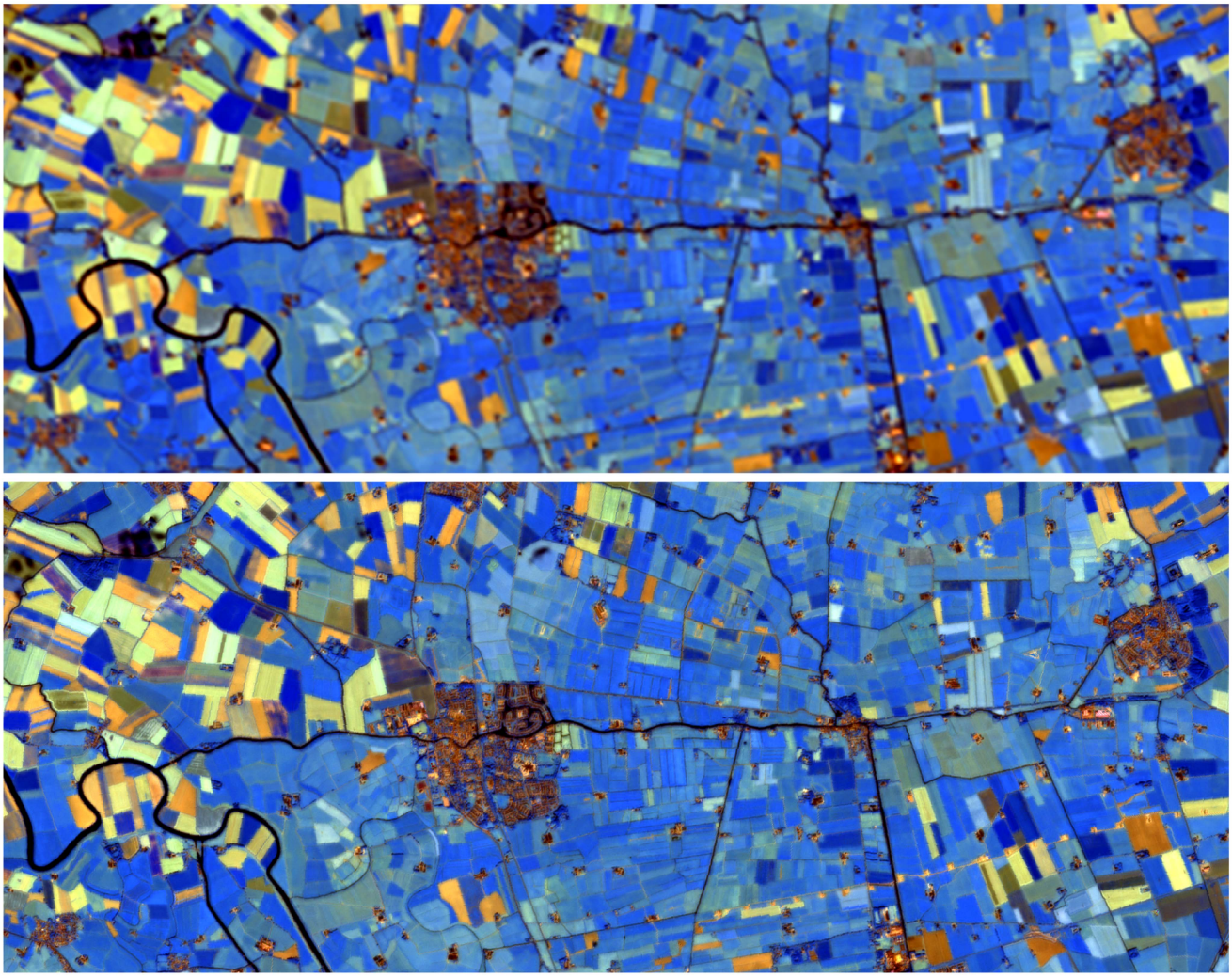

Fig. 7. (2105,1707,1004) nm EnMAP compositions: (top) 30 m-interpolated original; (bottom) hypersharpened.

index is calculated for the synthetic PAN of each HS band (2) and plotted versus the wavelength, as shown in Fig. 9. The index reflects the fraction of spatial information from the Sentinel-2 dataset that is incorporated into the fused HS dataset. The trend is rather flat, with the exception of small decrements toward the leftmost edge of the spectrum at 420 nm, due to quantum inefficiency, and at the rightmost edge of the visible spectrum. The average is close to 97.5% and indicates a high degree of spatial consistency. Again, the value of the index depends on the SNR of the original HS data, in the sense that low-SNR HS bands match the synthetic PAN to a lower extent.

The third and last index measures the intersensor consistency and is specific for the layout of spectral bands of Sentinel-2. The index reflects the ability of the hypersharpened EnMAP dataset to synthesize back the sharpening bands of Sentinel-2. With reference to Fig. 10, the determination coefficient, R^2, reaches a close unity value for all Sentinel-2 bands. Interestingly, the bands that are better synthesized are the large bands, for which more information comes from the hypersharpened HS dataset: red, NIR, far SWIR, and near SWIR. Conversely, consistency is lower for the narrower bands of the MS instrument: blue, green, the three RE's, and the narrow-band NIR (see Fig. 1). The lowest value of consistency is attained by the center RE band, of width 15 nm, which marks the spectral edge between absorption and reflection of vegetation. However, the average consistency is 96.9%, with a peak of 98%. The values of the index for the four large bands lie above the mean; below the mean, for the six narrow bands. The three 60-m bands are not considered because they are of no use for fusion with a 30-m HS dataset.

V. Conclusion and Development

We have shown that an HS observation can be merged with an auxiliary MS observation of the same scene of greater spatial resolution, taken at approximately the same date and time. The presence of PAN, together with either the HS image or the MS image, entails a further pansharpening step. Today, satellite HS missions provide approximately 220 narrow spectral bands at a spatial scale of 30 m. The ideal auxiliary MS dataset is provided

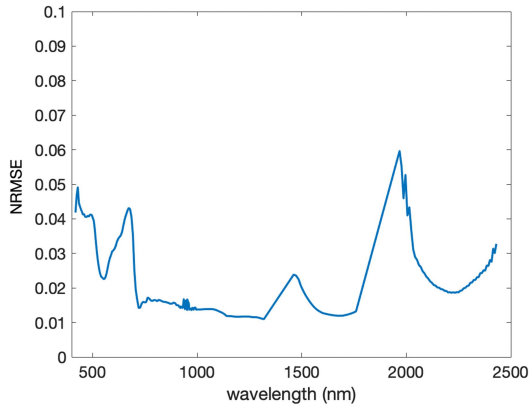

Fig. 8. Spectral consistency of EnMAP–Groningen: RMSE between original EnMAP bands and desharpened hypersharpened bands, normalized to the mean of the original band and plotted versus the wave length.

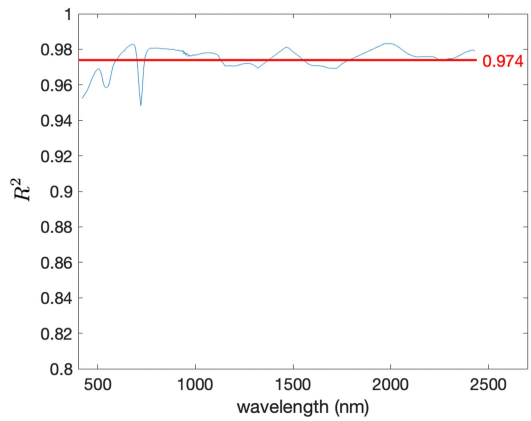

Fig. 9. Spatial consistency of EnMAP–Groningen toward the sharpening Sentinel-2 data: coefficient of determination of the multivariate regression of the hypersharpened HS bands to the sharpening combination of hypersharpened MS band, plotted versus the wave length. The average value, drawn in red, is 0.974.

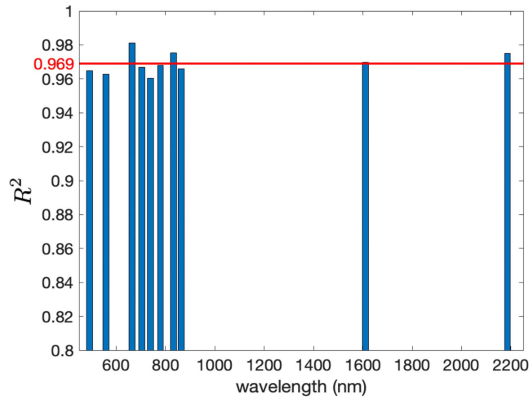

Fig. 10. Spectral consistency of EnMAP–Groningen toward the sharpening Sentinel-2 bands: coefficient of determination of the multivariate regression of the hypersharpened HS bands to the hypersharpened MS band of Sentinel-2. The average value, drawn in red, is 0.969.

by the Sentinel-2 twin-satellite constellation, with 10, 20, and 60 m spectral bands and a repetition capability of five days. Thus, EnMAP datacubes can be upgraded to 10 m resolution by means of two nested hypersharpening steps, the former performed on Sentinel-2 data only, to bring all its bands to 10 m, the latter on 30 m HS data that have been brought to 10 m. For the resolution enhancement of 30 m HS PRISMA data to a 5 m resolution, the proposed methods employ the two nested steps of hypersharpening, followed by a conventional pansharpening step. For PRISMA data, in which there is a reference of spatial quality, visual evaluations are corroborated by objective quality scores, carried out by means of established full-scale consistency indexes, chosen among those that exhibit good tolerance to misregistration. For EnMAP data, where the PAN image is missing, statistical intersensor consistence indexes have been developed to measure the improvement of the fused data over the original EnMAP and Sentinel-2 data.

The application scenario is for multiplatform fusion, but may also be for single-platform cases: WorldView-3, featuring PAN, VNIR, and SWIR, each at different scales, and OLI 100 m thermal, 30 m VNIR-SWIR, and 15 m PAN. It is evident that whenever we want to merge datasets having more than two different spatial scales, the classical pansharpening and hypersharpening methods cannot be used. The proposed approach is capable of tackling all such cases (WorldView-3, OLI), in addition to those addressed here.

The results of the proposed procedure are obtained with real-time processing, do not require parametric adjustments and/or training datasets, and are fully reproducible. We wish to recall that accurate instrumental, geometric, and atmospheric corrections are mandatory for the success of multiplatform hypersharpening. For the PRISMA HS test dataset, the two new consistency indexes provided average results, notwithstanding the fact that the fusion algorithm and the auxiliary sensor are the same.

The proposed approach may be useful for the temporal monitoring of vegetation [43], thanks to the regular availability of Sentinel-2 datasets every five days. In contrast, HS satellite observations are on demand; hence, they are expensive and necessarily sparse over time, also because of adverse meteorological conditions that can delay the planned acquisition. In principle, it would be possible to transplant the temporal repetition capability of Sentinel-2 MS data into the spectral resolution of HS data, to obtain many fused HS observations with only few original HS datasets.

Similarly to the fusion of Sentinel-2 and Sentinel-3 data [44], the fusion of EnMAP with Sentinel-2 would achieve an increase in both spatial and temporal resolutions. In a likely scenario, HS datasets are required only for substantial changes in vegetated land cover, more or less spaced over time, depending on the phenology of vegetation. Sentinel-2 datasets can be freely downloaded every five days, even if moderate cloud covers may limit their usability on some dates. The goal is to associate a group of Sentinel-2 images to a unique HS dataset and produce as many hypersharpened HS datasets, as the MS datasets are. There are no problems with spatial overlap because the swath of Sentinel-2 is ten times greater than that of any HS satellite instrument.

The sole extra task, which can be performed by experts or automatically, is the association of a temporarily contiguous segment of MS datasets with a unique HS dataset. Then, the latter is hypersharpened by means of each of the MS datasets of its group. Whenever the number of HS datasets of the same scene is low, also in the presence of critical phenological changes, it would be preferable to create as many HS datasets as there are MS ones. The temporal interpolation of the temporally rare HS pixel spectra should be driven by the phenological evolution of the scene, which in principle can be estimated from the MS spectra, coarsely sampled in wavelength, but more frequently in time. After that, the fusion is one-to-one: one true MS dataset shall sharpen one HS dataset, either true or interpolated, exactly as described in the present study.

ACKNOWLEDGMENT

The authors would like to thank the contribution of their former co-author, Dr. Claudia Zoppetti, who recently started a promising activity of technological transfer.

REFERENCES

[1] E. M. Middleton et al., "Hyperion: The first global orbital spectrometer, Earth Observing-1 (EO-1) satellite (2000–2017)," in *Proc. IEEE Int. Geosci. Remote Sens. Symp.*, 2017, pp. 3039–3042.

[2] R. Loizzo et al., "PRISMA: The Italian hyperspectral mission," in *Proc. IEEE Int. Geosci. Remote Sens. Symp.*, 2018, pp. 175–178.

[3] M. Habermeyer et al., "The EnMAP mission: From observation request to data delivery," in *Proc. IEEE Int. Geosci. Remote Sens. Symp.*, 2019, pp. 4507–4510.

[4] B. Aiazzi, L. Alparone, A. Barducci, S. Baronti, and I. Pippi, "Estimating noise and information of multispectral imagery," *Opt. Engin.*, vol. 41, no. 3, pp. 656–668, Mar. 2002.

[5] G. Vivone et al., "A critical comparison of pansharpening algorithms," in *Proc. IEEE Int. Geosci. Remote Sens. Symp.*, 2014, pp. 191–194.

[6] L. Alparone, B. Aiazzi, S. Baronti, and A. Garzelli, *Remote Sensing Image Fusion*. Boca Raton, FL, USA: CRC Press, 2015.

[7] M. Selva, B. Aiazzi, F. Butera, L. Chiarantini, and S. Baronti, "Hyper-sharpening: A first approach on SIM-GA data," *IEEE J. Sel. Topics Appl. Earth Observ. Remote Sens.*, vol. 8, no. 6, pp. 3008–3024, Jun. 2015.

[8] B. Aiazzi, L. Alparone, S. Baronti, and C. Lastri, "Crisp and fuzzy adaptive spectral predictions for lossless and near-lossless compression of hyperspectral imagery," *IEEE Geosci. Remote Sens. Lett.*, vol. 4, no. 4, pp. 532–536, Oct. 2007.

[9] M. S. Karoui, Y. Deville, F. Z. Benhalouche, and I. Boukerch, "Hypersharpening by joint-criterion nonnegative matrix factorization," *IEEE Trans. Geosci. Remote Sens.*, vol. 55, no. 3, pp. 1660–1670, Mar. 2017.

[10] M. Selva, L. Santurri, and S. Baronti, "Improving hypersharpening for WorldView-3 data," *IEEE Geosci. Remote Sens. Lett.*, vol. 16, no. 6, pp. 987–991, Jun. 2019.

[11] X. Lu, J. Zhang, X. Yu, W. Tang, T. Li, and Y. Zhang, "Hyper-sharpening based on spectral modulation," *IEEE J. Sel. Topics Appl. Earth Observ. Remote Sens.*, vol. 12, no. 5, pp. 1534–1548, May 2019.

[12] R. Restaino, G. Vivone, P. Addesso, and J. Chanussot, "Hyperspectral sharpening approaches using satellite multiplatform data," *IEEE Trans. Geosci. Remote Sens.*, vol. 59, no. 1, pp. 578–596, Jan. 2021.

[13] A. Garzelli, C. Zoppetti, A. Arienzo, and L. Alparone, "Spatial resolution enhancement of PRISMA hyperspectral data via nested hypersharpening with Sentinel-2 multispectral data," in *Proc. IEEE Int. Geosci. Remote Sens. Symp.*, 2023, pp. 5997–6000.

[14] J. Delegido, L. Alonso, G. González, and J. Moreno, "Estimating chlorophyll content of crops from hyperspectral data using a normalized area over reflectance curve (NAOC)," *Int. J. Appl. Earth Observ. Geoinf.*, vol. 12, no. 3, pp. 165–174, 2010.

[15] B. Johnson, "Effects of pansharpening on vegetation indices," *ISPRS Int. J. Geo-Inf.*, vol. 3, no. 4, pp. 507–522, Apr. 2014.

[16] A. Garzelli, B. Aiazzi, L. Alparone, S. Lolli, and G. Vivone, "Multispectral pansharpening with radiative transfer-based detail-injection modeling for preserving changes in vegetation cover," *Remote Sens.*, vol. 10, no. 8, pp. 1–18, Aug. 2018.

[17] L. Alparone, A. Arienzo, A. Garzelli, S. Lolli, and C. Zoppetti, "Fusion of optical and SAR satellite data for environmental monitoring: Assessment of damages and disturbances originated by forest fires," in *Proc. SPIE Conf. Image Signal Process. Remote Sens. XXVIII*, 2022, Art. no. 122670E.

[18] L. Alparone, A. Garzelli, and C. Zoppetti, "Fusion of VNIR optical and c-band polarimetric SAR satellite data for accurate detection of temporal changes in vegetated areas," *Remote Sens.*, vol. 15, no. 3, 2023, Art. no. 638.

[19] T. Sihvonen, Z.-S. Duma, H. Haario, and S.-P. Reinikainen, "Spectral profile partial least-squares (SP-PLS): Local multivariate pansharpening on spectral profiles," *ISPRS Open J. Photogramm. Remote Sens.*, vol. 10, 2023, Art. no. 100049.

[20] B. Aiazzi, L. Alparone, A. Garzelli, and L. Santurri, "Blind correction of local misalignments between multispectral and panchromatic images," *IEEE Geosci. Remote Sens. Lett.*, vol. 15, no. 10, pp. 1625–1629, Oct. 2018.

[21] B. Aiazzi, L. Alparone, F. Argenti, and S. Baronti, "Wavelet and pyramid techniques for multisensor data fusion: A performance comparison varying with scale ratios," in *Proc. SPIE Conf. Image Signal Process. Remote Sens.*, 1999, pp. 251–262.

[22] A. Garzelli, F. Nencini, L. Alparone, and S. Baronti, "Multiresolution fusion of multispectral and panchromatic images through the curvelet transform," in *Proc. IEEE Int. Geosci. Remote Sens. Symp.*, 2005, pp. 2838–2841.

[23] B. Aiazzi, L. Alparone, S. Baronti, R. Carlà, A. Garzelli, and L. Santurri, "Sensitivity of pansharpening methods to temporal and instrumental changes between multispectral and panchromatic data sets," *IEEE Trans. Geosci. Remote Sens.*, vol. 55, no. 1, pp. 308–319, Jan. 2017.

[24] L. Alparone, A. Garzelli, and G. Vivone, "Intersensor statistical matching for pansharpening: Theoretical issues and practical solutions," *IEEE Trans. Geosci. Remote Sens.*, vol. 55, no. 8, pp. 4682–4695, Aug. 2017.

[25] A. Arienzo, B. Aiazzi, L. Alparone, and A. Garzelli, "Reproducibility of pansharpening methods and quality indexes versus data formats," *Remote Sens.*, vol. 13, no. 21, pp. 1–21, Oct. 2021.

[26] F. Pacifici, N. Longbotham, and W. J. Emery, "The importance of physical quantities for the analysis of multitemporal and multiangular optical very high spatial resolution images," *IEEE Trans. Geosci. Remote Sens.*, vol. 52, no. 10, pp. 6241–6256, Oct. 2014.

[27] S. Lolli and P. Di Girolamo, "Principal component analysis approach to evaluate instrument performances in developing a cost-effective reliable instrument network for atmospheric measurements," *J. Atmos. Ocean. Technol.*, vol. 32, no. 9, pp. 1642–1649, Sep. 2015.

[28] M. Ciofini, A. Lapucci, and S. Lolli, "Diffractive optical components for high power laser beam sampling," *J. Opt. A: Pure Appl. Opt.*, vol. 5, no. 3, pp. 186–191, May 2003.

[29] S. Lolli, L. Alparone, A. Garzelli, and G. Vivone, "Haze correction for contrast-based multispectral pansharpening," *IEEE Geosci. Remote Sens. Lett.*, vol. 14, no. 12, pp. 2255–2259, Dec. 2017.

[30] P. S. Chavez Jr., "Image-based atmospheric corrections–revisited and improved," *Photogramm. Eng. Remote Sens.*, vol. 62, no. 9, pp. 1025–1036, Sep. 1996.

[31] G. Vivone, A. Arienzo, M. Bilal, A. Garzelli, G. Pappalardo, and S. Lolli, "A dark target Kalman filter algorithm for aerosol property retrievals in urban environment using multispectral images," *Urban Climate*, vol. 43, pp. 1–17, May 2022.

[32] Q. Fu and K. N. Liou, "On the correlated k-distribution method for radiative transfer in nonhomogeneous atmospheres," *J. Atmos. Sci*, vol. 49, no. 22, pp. 2139–2156, Nov. 1992.

[33] G. Vivone, A. Garzelli, Y. Xu, W. Liao, and J. Chanussot, "Panchromatic and hyperspectral image fusion: Outcome of the 2022 WHISPERS hyperspectral pansharpening challenge," *IEEE J. Sel. Topics Appl. Earth Observ. Remote Sens.*, vol. 16, pp. 166–179, Nov. 2022.

[34] B. Aiazzi, S. Baronti, and M. Selva, "Improving component substitution pansharpening through multivariate regression of MS pan data," *IEEE Trans. Geosci. Remote Sens.*, vol. 45, no. 10, pp. 3230–3239, Oct. 2007.

[35] G. Vivone, L. Alparone, A. Garzelli, and S. Lolli, "Fast reproducible pansharpening based on instrument and acquisition modeling: AWLP revisited," *Remote Sens.*, vol. 11, no. 19, pp. 1–23, Oct. 2019.

[36] B. Aiazzi, L. Alparone, S. Baronti, A. Garzelli, and M. Selva, "Advantages of Laplacian pyramids over "à trous" wavelet transforms for pansharpening of multispectral images," in *Proc. SPIE Conf. Image. Signal Process. Remote Sens. XVIII*, 2012, pp. 853704-1–853704-10.
[37] B. Aiazzi, L. Alparone, S. Baronti, and R. Carlà, "Assessment of pyramid-based multisensor image data fusion," in *Proc. SPIE Conf. Image Signal Process. Remote Sens. IV*, 1998, pp. 237–248.
[38] F. Palsson, J. R. Sveinsson, M. O. Ulfarsson, and J. A. Benediktsson, "Quantitative quality evaluation of pansharpened imagery: Consistency versus synthesis," *IEEE Trans. Geosci. Remote Sens.*, vol. 54, no. 3, pp. 1247–1259, Mar. 2016.
[39] A. Arienzo, G. Vivone, A. Garzelli, L. Alparone, and J. Chanussot, "Full-resolution quality assessment of pansharpening: Theoretical and hands-on approaches," *IEEE Geosci. Remote Sens. Mag.*, vol. 10, no. 3, pp. 2–35, Sep. 2022.
[40] X. Guan, F. Li, X. Zhang, M. Ma, and S. Mei, "Assessing full-resolution pansharpening quality: A comparative study of methods and measurements," *IEEE J. Sel. Topics Appl. Earth Observ. Remote Sens.*, vol. 16, pp. 6860–6875, Jul. 2023.
[41] A. Arienzo, L. Alparone, A. Garzelli, and S. Lolli, "Advantages of nonlinear intensity components for contrast-based multispectral pansharpening," *Remote Sens.*, vol. 14, no. 14, 2022, Art. no. 3301.
[42] L. Alparone, A. Garzelli, and G. Vivone, "Spatial consistency for full-scale assessment of pansharpening," in *Proc. IEEE Int. Geosci. Remote Sens. Symp.*, 2018, pp. 5132–5134.
[43] M. A. Cho and A. K. Skidmore, "A new technique for extracting the red edge position from hyperspectral data: The linear extrapolation method," *Remote Sens. Environ.*, vol. 101, no. 2, pp. 181–193, 2006.
[44] Q. Wang and P. M. Atkinson, "Spatio-temporal fusion for daily Sentinel-2 images," *Remote Sens. Environ.*, vol. 204, pp. 31–42, 2018.

Luciano Alparone received the Laurea (M.Sc.) degree with honors in electronic engineering from the University of Florence, Florence, Italy, in 1985, and the Ph.D. degree in telecommunications and information science from the Italian Ministry of Education, University and Research, Rome, Italy, in 1990.

Since 2002, he has been an Associate Professor with the Department of Information Engineering (DINFO, after 2011), University of Florence. He is presently a Full Professor of telecommunications and Head of the Signal Processing and Telecommunications Lab. (LENST). He has authored or coauthored about 100 papers in peer-reviewed journals and a total of more than 300 publications. He has been the Principal Author of the book titled *Remote Sensing Image Fusion* (CRC Press, Taylor & Francis Group, Boca Raton, FL, USA, in March 2015). His research interests include data compression for remote sensing applications, multiresolution image analysis and processing, multisensor image fusion, and analysis and processing of SAR images.

Dr. Alparone was the recipient of the 2004 IEEE GEOSCIENCE AND REMOTE SENSING LETTERS Prize Paper Award for the study on "A global quality measurement of pansharpened multispectral imagery." He is listed in both career-long and single-year (2019 onward) World's Top 2% Scientists by Stanford University.

Alberto Arienzo received the B.S. and M.S. degrees in telecommunications engineering and the Ph.D. degree in information engineering, from the University of Florence, Florence, Italy, in 2012, 2015, and 2023, respectively.

From 2018 to 2022, he was with the Institute of Applied Physics "Nello Carrara" (IFAC-CNR), National Research Council of Italy. Since 2023, he has been with OHB System AG, Oberpfaffenhofen, Germany, as a Performance and Calibration System Engineer of electro-optical sensors related to remote sensing. His research interests include remote sensing, imagery science, and multisensor data fusion.

Andrea Garzelli (Senior Member, IEEE) received the Laurea degree (summa cum laude) in electronic engineering and the Ph.D. degree in information and telecommunications engineering from the University of Florence, Florence, Italy, in 1991 and 1995, respectively.

He is a Professor of telecommunications with the Department of Information Engineering and Mathematics, University of Siena, Siena, Italy, where he holds the courses of fundamentals of signal processing and telecommunications, statistical signal processing, and remote sensing. He has coauthored the book *Remote Sensing Image Fusion* (CRC Press, 2015). His research interests include image analysis and classification with applications to image fusion for optical and synthetic aperture radar images.

Dr. Garzelli is a Member of the IEEE Geoscience and Remote Sensing Society. He was the recipient of the IEEE GEOSCIENCE AND REMOTE SENSING LETTERS Prize Paper Award in 2004, and also of the Best Reviewers of IEEE TRANSACTIONS ON GEOSCIENCE AND REMOTE SENSING in 2014, a journal for which he has been an Associate Editor since 2015. He has been recognized in Stanford University's list of the World's Top 2% Scientists for the single years 2019, 2020, 2021, 2022, and for his entire career.

Open Access funding provided by 'Università degli Studi di Siena' within the CRUI CARE Agreement